



Article

Study of Cathode Materials for Na-Ion Batteries: Comparison Between Machine Learning Predictions and Density Functional Theory Calculations

Claudio Ronchetti ¹, Sara Marchio ², Francesco Buonocore ^{2,*}, Simone Giusepponi ², Sergio Ferlito ³ and Massimo Celino ²

¹ Telespazio S.p.A., Via Tiburtina 965, 00156 Rome, Italy; claudio.ronchetti@telespazio.com

² Italian National Agency for New Technologies, Energy and Sustainable Economic Development (ENEA)—C. R. Casaccia, Via Anguillarese 301, 00123 Rome, Italy; sara.marchio@enea.it (S.M.); simone.giusepponi@enea.it (S.G.); massimo.celino@enea.it (M.C.)

³ Italian National Agency for New Technologies, Energy and Sustainable Economic Development (ENEA)—C. R. Portici, Piazzale Enrico Fermi 1, 80055 Portici, Italy; sergio.ferlito@enea.it

* Correspondence: francesco.buonocore@enea.it

Abstract: Energy storage technologies have experienced significant advancements in recent decades, driven by the growing demand for efficient and sustainable energy solutions. The limitations associated with lithium's supply chain, cost, and safety concerns have prompted the exploration of alternative battery chemistries. For this reason, research to replace widespread lithium batteries with sodium-ion batteries has received more and more attention. In the present work, we report cutting-edge research, where we explored a wide range of compositions of cathode materials for Na-ion batteries by first-principles calculations using workflow chains developed within the AiiDA framework. We trained crystal graph convolutional neural networks and geometric crystal graph neural networks, and we demonstrate the ability of the machine learning algorithms to predict the formation energy of the candidate materials as calculated by the density functional theory. This materials discovery approach is disruptive and significantly faster than traditional physics-based computational methods.

Keywords: DFT calculations; neural networks; machine learning; electrochemical energy storage; Na-ion; high-throughput calculations



Citation: Ronchetti, C.; Marchio, S.; Buonocore, F.; Giusepponi, S.; Ferlito, S.; Celino, M. Study of Cathode Materials for Na-Ion Batteries: Comparison Between Machine Learning Predictions and Density Functional Theory Calculations. *Batteries* **2024**, *10*, 431. <https://doi.org/10.3390/batteries10120431>

Academic Editor: Shaokun Chong

Received: 30 September 2024

Revised: 27 November 2024

Accepted: 3 December 2024

Published: 5 December 2024



Copyright: © 2024 by the authors. Licensee MDPI, Basel, Switzerland. This article is an open access article distributed under the terms and conditions of the Creative Commons Attribution (CC BY) license (<https://creativecommons.org/licenses/by/4.0/>).

1. Introduction

As global technology advances, humanity faces significant challenges in terms of pollution and climate impact. The current trajectory is unsustainable; while technological progress improves our quality of life, it simultaneously endangers the planet. A critical shift is necessary, from relying on fossil fuels like oil and coal for energy production to adopting renewable energy sources [1]. Renewable energy primarily involves converting power from the Sun, wind, and oceans into electricity. However, these energy sources do not incessantly produce power, creating a need for effective energy storage solutions.

Lithium-ion batteries (LIBs) have been highly successful in meeting energy storage demands in recent years [2]. Yet, with the growing energy needs, particularly in sectors like transportation where the shift from fossil fuels to electricity is accelerating, LIBs face two major challenges: an increase in the cost of Li due to its limited availability with respect to the increasing demand; and safety concerns related to the reactivity of lithium with oxygen. Sodium-ion batteries (NIBs) offer a promising alternative to LIBs. Sodium is abundant and more stable than lithium, making NIBs an attractive option [3]. Additionally, NIBs are safer than LIBs due to sodium's lower reactivity compared to lithium, which mitigates the risks associated with flammable batteries. Actually, NIBs are rechargeable batteries analogous

to LIBs, in which both cathodes use the intercalation reaction mechanism. Sodium-based cathodes have high operating potentials and high capacities, potentially comparable to lithium-based ones [4–7]. Consequently, the combination of strong performance and lower costs, along with the ability to leverage existing technology and production methods developed for LIBs without incurring additional expenses, has fueled growing interest in these systems.

Sodium cathode material based on layered transition metal (M) oxide (LTMO), Na_xMO_2 , is one of the more promising classes of materials to consider [8,9]. Indeed, Na_xMO_2 materials exhibit reversible phase transitions that enhance the stability of batteries during charge–discharge cycles. LTMO is classified as $\text{O}_{3-\text{P}3}$ and $\text{P}2-\text{O}2$ depending on its octahedral and prismatic crystal phase, respectively, where n counts the number of transition metal layers in the unit cell. It has been found that the $\text{O}_{3-\text{P}3}$ and $\text{P}2-\text{O}2$ phase transitions do not break the M–O bond during the electrochemical cycle, saving the cathode from damages. However, the $\text{P}2-\text{O}2$ phase transition requires a minimal transformation of the crystal, preserving the structural integrity of the $\text{P}2$ -type phase and ensuring robust cycling stability. Moreover, the spacing between the metal layers is larger in the $\text{P}2$ - than in the $\text{O}3$ -type phase, allowing the enhancement of the Na^+ -ion's mobility. On the other hand, the $\text{O}3$ -type phase can suffer complex distortion during the charge–discharge process.

Different strategies have been proposed to increase the density of energy and to enhance stability, preventing Jahn–Teller distortions [10,11] in NIB LTMO cathode materials, including structural modulation, surface modification, and elemental doping [12–16].

Machine learning (ML) has become a widely utilized technique, enabling researchers to accelerate their work using trained algorithms. In materials science, ML is applied to predict material properties, significantly reducing the time and computational resources needed compared to traditional numerical physical models, which are often resource-intensive and rely on modern supercomputers [17]. In the present work, we propose a computational study to enhance the stability of Na_xMnO_2 cathode materials by the substitutional doping of Mn elements with two different methods: (1) high-throughput first principles calculations based on density functional theory (DFT); and (2) machine learning techniques based on the training of a convolutional neural network (CNN) from a dataset generated by DFT calculations. The stability is established by the DFT calculations or CNN predictions to determine the formation energy (more stable crystals have lower formation energy). We compare the two methods to assess the predictive capability of the CNN upon training.

Our previous work [18] provided details on the ML methodology and computational architecture employed to predict the formation energy using the Materials Project dataset. The design, training process, and computational tools utilized to achieve accurate predictions on the dataset have been illustrated. However, the focus of the present work diverges from this approach. Instead of exploring the initial training and methodology, this study aims to evaluate the performance of the pre-trained model on an entirely different dataset that was not included in the original training phase. Specifically, the assessment centers on NIB systems, chosen for their distinctive properties, to determine the extent to which the pre-trained model is capable of generalizing to new and unseen data. By doing so, this work seeks to validate the robustness and transferability of the pre-trained model, offering insights into its broader applicability and limitations when applied to diverse datasets.

2. Materials and Methods

2.1. Base Crystal NaMnO_2 and Doping

The $\text{P}2$ -type crystal cathode materials of the present study were generated from the base $\text{P}2\text{-NaMnO}_2$ crystal by the substitution of randomly selected Mn atoms with the first-row transition metals Ni and Ti. The procedure of the substitution is shown in Section 2.3 (Computational Workflow). The base crystal where the Mn atoms were substituted was created as the supercell $3 \times 2 \times 1$ of the crystal mp-971647 of the Materials Project database [19] so that 48 atoms were present therein. Preliminary studies indicated

that Ti substitution enables the better optimization of the stability and intercalation potential compared to other elements such as V, Cr, Cu, Fe, and Zn [18].

2.2. First-Principles Method

To characterize the structural and electronic properties of the materials under study, a first-principles approach was adopted using the Plane-Wave Self-Consistent Field (PWSCF) code, which is based on density functional theory and is part of the Quantum ESPRESSO suite [20,21]. The PWSCF code conducts various types of self-consistent calculations of electronic structural properties within the framework of DFT [22,23], utilizing a plane-wave (PW) basis set and pseudopotentials (PP).

The electron–ion interaction was described using Rappe–Rabe–Kaxiras–Joannopoulos ultrasoft pseudopotentials with nonlinear core correction, while the exchange–correlation energies were modeled using the generalized gradient approximation (GGA) with the Perdew–Burke–Ernzerhof (PBE) functional [24]. A total of 9, 15, 6, 12, and 10 electrons were explicitly considered in the wave functions for Na, Mn, O, Ti, and Ni, respectively. The electronic wave functions were expanded using a plane-wave basis set with a kinetic energy cut-off of 80 Ry, while the charge density cutoff was set to 640 Ry (eight times greater). A $4 \times 4 \times 4$ Monkhorst-Pack k-point mesh [25] was employed. Additionally, Marzari–Vanderbilt smearing [26] with a width of 0.01 Ry was applied. In our calculations, we considered the spin polarization. Although the generalized gradient approximation (GGA) approach provides accurate predictions for many materials' properties, it is not consistently reliable for all cases. Specifically, GGA functionals struggle with accurately describing electronic correlations in the partially occupied 3d, 4d, and 5d shells of transition metals. This limitation often leads to the underestimation of the energy band gap in transition metal oxides. To address this issue, the Hubbard U self-interaction correction (DFT + U method) was adopted to consider the d-orbitals correlation [27]. We assumed the values $U_{\text{Mn}} = 4.7$ eV, $U_{\text{Ni}} = 6.95$ eV, and $U_{\text{Ti}} = 3.22$ eV for the Hubbard parameters.

Periodic boundary conditions (PBC), which allow for the simulation of an infinitely extended system, were applied in all calculations in combination with the supercell approximation. To determine reliable values for the kinetic energy cutoff, k-point sampling, and smearing width, preliminary test calculations were performed on the pseudopotentials. Total energy, forces, and stress were verified to match the tolerances of 0.001 Ry/atom, 0.0001 Ry/Bohr, and 0.1 kbar, respectively. The conjugate gradient (CG) minimization method was employed for energy minimization, with a convergence threshold for self-consistency set at 10^{-6} Ry. The Broyden–Fletcher–Goldfarb–Shanno (BFGS) quasi-Newton algorithm was used for geometry optimization, which was considered achieved when the following two conditions were met: (i) the energy change between two consecutive self-consistent field (SCF) steps was less than 10^{-4} Ry, and (ii) the maximum force acting on an atom was less than 10^{-3} Ry/Bohr. We also used the BFGS quasi-Newton algorithm for variable cell relaxation, adding the additional condition that all components of the stress tensor should be smaller than 0.05 GPa.

To evaluate the impact of the doping in the starting structure (P2-layered oxide NaMnO_2), several structures were built by replacing the Mn atoms (from 1 up to 12) with Ti and Ni atoms. These systems were inspected by calculating the formation energy.

The formation energy E_f is calculated by using the following formula:

$$E_f = \frac{E_{\text{sys}}^{\text{tot}} - n_{\text{Na}}E_{\text{Na}}^{\text{bulk}} - n_{\text{Mn}}E_{\text{Mn}}^{\text{bulk}} - n_{\text{Ti}}E_{\text{Ti}}^{\text{bulk}} - n_{\text{Ni}}E_{\text{Ni}}^{\text{bulk}} - \frac{1}{2}n_{\text{O}}E_{\text{O}_2}}{N_{\text{tot}}} \quad (1)$$

where $E_{\text{sys}}^{\text{tot}}$ is the total energy of the system, N_{tot} is the total number of atoms contained in the supercell, E_X^{bulk} is the total energy per atom of the species X (Na, Mn, Ti, and Ni) in the most stable bulk phase, E_{O_2} is the total energy of the oxygen molecule, and n_X is the number of atoms of the species X (Na, Mn, Ti, Ni, and O).

2.3. Computational Workflow

The search for optimal cathodic materials in terms of formation energy was addressed here through the systematic screening of numerous materials. To validate the ML model, the values obtained through artificial intelligence (AI) for the formation energy were compared with their counterparts obtained through the DFT calculations, which were conducted for each of the candidates. These DFT calculations, as well as the methodologies employed to generate material variants, were based on well-established procedures, and this circumstance made it possible to automate and integrate them within a computational workflow chain (workchain).

A workchain can be defined as the total or partial automation of a work process, divided into simpler tasks processed sequentially or in parallel according to a logical model. The workchain employed here for the screening of potential cathodic materials was developed within the AiiDA (Automated Interactive Infrastructure and Database) framework [28–30], an open-source workflow management system devised for computational science. The AiiDA infrastructure is implemented in the Python language and has interfaces that allow it to be flexible. The management of DFT calculations within the workflow described here was performed using the plugin for the Quantum ESPRESSO code [31].

The workflow implementation was based on the AiiDA workchain object, which manages the execution of multiple long-duration calculations through the definition of sub-units called steps, ensuring that progress is not lost in case of sudden interruptions.

The tasks for each step are schematically depicted in Figure 1. They consist of the following:

1. Random generator. This involves creating a variation from the starting structure in a random way. Starting from the initial structure S_0 (NaMnO_2), alternative structures are randomly generated by applying one or more rules. The rules adopted can be summarized as follows.
 - Doping via the replacement of manganese atoms with transition metals. This rule takes, as the input, the initial structure S_0 , a list of N_{tm} transition metals, the minimum number of manganese atoms to be maintained within the structure $\min_{(\#Mn)}$, and multiplier $steps$ that define the number of atoms to be replaced at a time. The output is S_1 , a structure varied by replacing some of the manganese atoms with transition metals belonging to the list of the N_{tm} transition metals. The site positions of the manganese atoms to be replaced are randomly chosen. The number of the replaced manganese atoms is also randomly chosen such that the number of manganese atoms in S_1 is greater or equal to $\min_{(\#Mn)}$.
 - Variation in the number of intercalated ions to define structures with fewer or no sodium atoms. This rule takes as the input the initial structure S_0 . The output is S_1 , a structure varied by removing a randomly chosen number of sodium atoms.
2. Symmetry equivalence check. The symmetry equivalence check task compares the structure generated by the random generator task with all the structures for which the calculation has already been performed to determine whether the structures are symmetrically equivalent. The algorithm is based on the open-source solution reported in the ref. [32] that was implemented in the Python tool Atomic Simulation Environment (ASE) [33].
3. Computing procedure. The computing procedure task submits the DFT + U calculation jobs to the ENEA HPC computing infrastructure [34] to extract the quantities of interest for this study.
4. Data store. The data store task stores the results of the DFT + U calculation in the AiiDA database and in an external Mongo DB instance. To accomplish this, the task consists of two parts:
 - Adapter. This organizes the data extracted from the parser into the chosen format (json in our case).

- Uploader. This loads the data with the new format into the database.

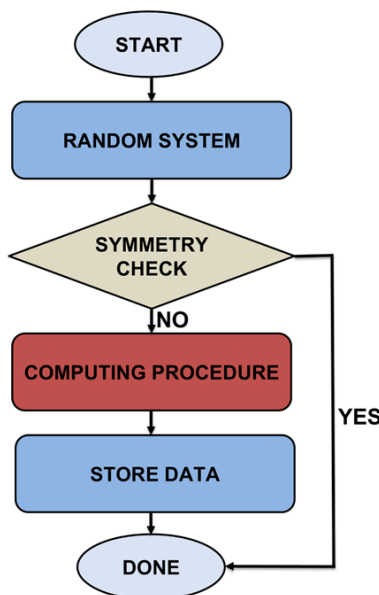


Figure 1. A flowchart of the workchain tasks as implemented in the AiiDA framework.

2.4. Machine Learning Method

In this study, we explored a wide combinatorial space of material candidates for cathode batteries by generating numerous alternatives through the random substitution of crystal elements. To evaluate the properties of this extensive dataset, consisting of systems generated by doping the initial NaMnO_2 structure, we adopted a data-driven approach. The geometric crystal graph neural network (GeoCGNN) [35] was used to predict the formation energies of the crystals. The GeoCGNN enhances the earlier crystal graph convolutional neural network (CGCNN) [36] version by integrating detailed spatial geometric information into the model. Both the CGCNN and GeoCGNN architectures leverage message-passing neural networks (MPNNs) [37] and gated convolution.

The input of the GeoCGNN model is a graph generated on top of the crystal structure provided as a crystallographic information file (CIF) where the nodes represent the atoms in the crystal and the edges represent the interactions between them. The edges are defined for atoms separated by less than 8 Å, with a maximum of 12 neighbors considered for each atom. The nodes are encoded as one-hot feature vectors based on atomic properties, while the edge feature vectors are the distance vectors between interacting atoms. Additionally, the model incorporates descriptors that encode lattice vectors and the cell volume. The output is typically a scalar property of the material. In this case, the target property is the formation energy.

The network was trained on a large dataset of materials obtained from the Materials Project (MP) database [19], excluding only structures containing noble gasses. The data were stored on Red Hat Ceph Storage [38], a solution tailored for data analytics and artificial intelligence. We used 80% of the dataset, comprising 126,162 materials, for training, with the remaining 20% split equally for validation and testing. The training process utilized the Stochastic Gradient Descent (SGD) [39] method with a learning rate of 0.001, a batch size of 64, and mean squared error (MSE) as the loss function for the regression task. The training ran for a maximum of 500 epochs, with the best-performing hyperparameters selected based on validation error.

During the inference phase, the trained model was used to estimate the formation energies of the candidate material for cathode batteries. A total of 8071 crystal structures were randomly generated based on the rules outlined in Section 2.3 (Computational Workflow). Since these new structures are not present in the MP database, DFT calculations were

performed to compare the obtained formation energy values with those predicted by the model. To efficiently manage the large number of materials, both the random generation of crystal structures and the DFT calculations were automated using the workflow detailed in the previous section (Section 2.3).

3. Results and Discussion

3.1. Base Crystal Structure

As we have reported above, the NaMnO_2 base crystal was modeled using the supercell $3 \times 2 \times 1$ of the crystal mp-971647 of the Materials Project database [19]. The resulting supercell was monoclinic with $a = 9.30 \text{ \AA}$; $b = 6.20 \text{ \AA}$; $c = 10.90 \text{ \AA}$; $\alpha = 90^\circ$; $\beta = 90^\circ$; $\gamma = 120^\circ$; and $N_{\text{tot}} = 48$ atoms (12 Na atoms, 12 Mn atoms, and 24 O atoms), as depicted in Figure 2. In this P2-layered oxide, the Na and Mn layers alternated at a distance of 2.73 \AA (the distance between layers of the same type was doubled at 5.45 \AA). Each Mn layer had two O layers (above and below) at a distance of 0.95 \AA . The Na layer formed a hexagonal structure with a side $a_{\text{Na}} = 3.10 \text{ \AA}$ in which each Na atom had six Na atoms at distance $d_{\text{Na-Na}} = a_{\text{Na}}$, and the stacking sequence was ABA. Equally, the Mn layer formed the same hexagonal structure but with an overlapping stacking sequence ($d_{\text{Mn-Mn}} = a_{\text{Mn}} = 3.10 \text{ \AA}$). Each Na(Mn) atom had six Mn(Na) at a distance of $d_{\text{Na-Mn}} = 3.26 \text{ \AA}$ and had six O atoms at a distance of $d_{\text{Na-O}} = 2.52 \text{ \AA}$ ($d_{\text{Mn-O}} = 2.03 \text{ \AA}$). Upon the substitution of randomly selected Mn atoms, each supercell geometry was fully relaxed, allowing for the optimization of the cell parameters (variable cell relax). As an example, here we report the cell parameters of the base crystal with the Na-ions. Upon the cell relaxation, the structure distorted, increasing the volume by about 2.6% and losing its hexagonal shape. The cell parameters were $a = 9.77 \text{ \AA}$; $b = 5.86 \text{ \AA}$; $c = 10.92 \text{ \AA}$; $\alpha = 90^\circ$; $\beta = 90^\circ$; and $\gamma = 116.7^\circ$. The Na and Mn layers' distance remained the same, but the O layers increased their distance from the Mn layers up to 1.12 \AA . The Na(Mg) layers lost the hexagonal symmetry and then each Na(Mn) atom had two Na(Mn) atoms at $d_{\text{Na-Na}} (d_{\text{Mn-Mn}}) = 2.93 \text{ \AA}$ and four Na(Mn) atoms at $d_{\text{Na-Na}} (d_{\text{Mn-Mn}}) = 3.26 \text{ \AA}$. Likewise, two pairs of Na-Mn atoms approached each other, reducing their distance at $d_{\text{Na-Mn}} = 3.23 \text{ \AA}$, while four pairs of Na-Mn atoms moved apart each other, increasing their distance at $d_{\text{Na-Mn}} = 3.32 \text{ \AA}$. For the oxygen, the situation was the opposite, as the distance was reduced to $d_{\text{Mn-O}} = 1.97 \text{ \AA}$ for four pairs of Mn-O atoms and was increased to $d_{\text{Mn-O}} = 2.49 \text{ \AA}$ for two pairs of Mn-O atoms. The distances between the Na and O atoms were reduced to $d_{\text{Na-O}} = 2.41 \text{ \AA}$ for four pairs and to $d_{\text{Na-O}} = 2.47 \text{ \AA}$ for two pairs.

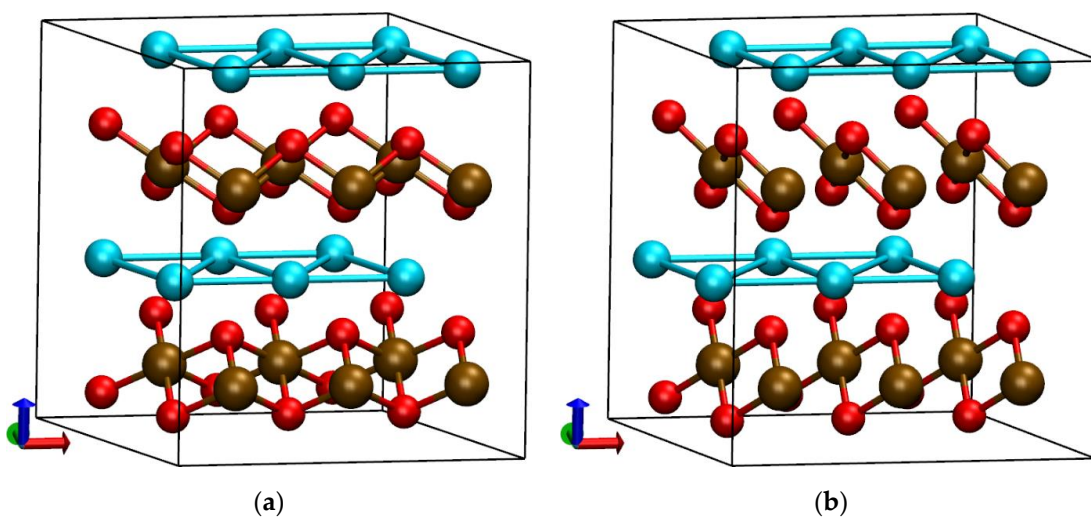


Figure 2. Starting non-relaxed (a) and relaxed (b) configurations of P2-layered oxide MnNaO_2 system. In light blue, brown, and red are Na, Mn, and O atoms, respectively.

3.2. Formation Energy

The formation energy was calculated using Equation (1) for the base crystal NaMnO_2 ; E_f was -2.01 eV for the non-relaxed system and -2.12 eV for the relaxed one. To make a comparison between the predicted and actual formation energies, it was necessary to create a test dataset useful for this case. Creating a good test dataset is crucial for evaluating the performance and the generalizability of a deep learning (DL) model.

Firstly, the test dataset should represent the entire distribution of data that the DL model will encounter in common usage [40,41]. If the test dataset does not represent the diversity of the real usage, the evaluation metrics will be misleading. AiiDA workflow rules have made it possible to represent this diversity by creating a balanced dataset.

Secondly, the test dataset should be large enough to provide reliable performance estimates [40,42]. This was difficult to achieve because of the long times required for the simulations. Despite these difficulties, the dataset contained more than 500 calculations.

Lastly, it should be ensured that the test dataset does not include information from the training dataset [40,41]. In this case, none of our calculated systems were stored in Materials Project database.

The test dataset was created with all these principles in mind by using the AiiDA workflow. In Figure 3, we compare and validate predictions from our ML method with results from the DFT calculations. On the left, the predictions of E_f for the 8071 non-relaxed crystal structures randomly generated are depicted in gray circles, showing a negative range of values between -3 eV and -1 eV. Moreover, some systems are highlighted by circles of different colors and labeled with their specific composition. This evidences that titanium doping increased the stability of the system (more negative E_f), while nickel doping reduced it (less negative E_f). Indeed, $\text{Na}_{12}\text{Ti}_{12}\text{O}_{24}$ (violet circle) was the system with the lowest E_f (-2.78 eV); conversely, $\text{Na}_{12}\text{Ni}_{12}\text{O}_{24}$ was the system (dark green circle) with the highest value of E_f (-1.20 eV). The base crystal $\text{Na}_{12}\text{Mn}_{12}\text{O}_{24}$ (black circle), placed in the middle of the range (-1.88 eV), was in an intermediate state of stability. The substitution of one manganese atom with a titanium atom ($\text{Na}_{12}\text{Mn}_{11}\text{TiO}_{24}$; red circle; $E_f = -1.97$ eV) decreased the formation energy by 0.09 eV, thereby increasing the system's stability. Conversely, the substitution of a manganese atom with a nickel atom ($\text{Na}_{12}\text{Mn}_{11}\text{NiO}_{24}$; brown circle; $E_f = -1.84$ eV) increased the formation energy by 0.04 eV, making the structure less stable. In Figure 3, predictions are also reported for the system $\text{Na}_{12}\text{Mn}_4\text{Ni}_4\text{Ti}_4\text{O}_{24}$ (orange circles) with an equal composition of the three transition metals (Mn, Ti, and Ni) and for the systems in which two transition metals have the same concentration, i.e., $\text{Na}_{12}\text{Mn}_3\text{Ni}_6\text{Ti}_3\text{O}_{24}$ (magenta circles), $\text{Na}_{12}\text{Mn}_6\text{Ni}_3\text{Ti}_3\text{O}_{24}$ (green circles), and $\text{Na}_{12}\text{Mn}_3\text{Ni}_3\text{Ti}_6\text{O}_{24}$ (light blue circles). Since, for these compositions, there were several different configurations, in addition to the range of the variability in the formation energy, the mean value $\langle E_f \rangle$ and the standard deviation σ_{E_f} were calculated to evaluate statistical uncertainty. For the $\text{Na}_{12}\text{Mn}_4\text{Ni}_4\text{Ti}_4\text{O}_{24}$ system, the range was from -2.10 to -2.00 eV; $\langle E_f \rangle = -2.06$ eV; and $\sigma_{E_f} = 0.01$ eV. For the $\text{Na}_{12}\text{Mn}_3\text{Ni}_6\text{Ti}_3\text{O}_{24}$ system, the range was from -1.87 to -1.80 eV; $\langle E_f \rangle = -1.85$ eV; and $\sigma_{E_f} = 0.01$ eV. For the $\text{Na}_{12}\text{Mn}_6\text{Ni}_3\text{Ti}_3\text{O}_{24}$ system, the range was from -2.05 to -1.98 eV; $\langle E_f \rangle = -2.02$ eV; and $\sigma_{E_f} = 0.02$ eV. For the $\text{Na}_{12}\text{Mn}_3\text{Ni}_3\text{Ti}_6\text{O}_{24}$ system, the range was from -2.30 to -2.24 eV; $\langle E_f \rangle = -2.27$ eV; and $\sigma_{E_f} = 0.01$ eV. In Figure 3, statistical uncertainty is indicated by black solid lines centered in the mean values and limited by the standard deviations. On the right side of Figure 3, the calculated values of the formation energy of the non-relaxed systems using the first-principles method are shown by colored cross symbols. At least one of the systems highlighted on the left in the figure was analyzed by DFT calculations by evaluating its formation energy. Notably, we see that the same order of stability as the predicted formation energy was found. The $\text{Na}_{12}\text{Ti}_{12}\text{O}_{24}$ system (violet cross) was the most stable, with $E_f = -2.52$ eV; the $\text{Na}_{12}\text{Ni}_{12}\text{O}_{24}$ (dark green cross) system was the least stable, with $E_f = -1.15$ eV. The base crystal $\text{Na}_{12}\text{Mn}_{12}\text{O}_{24}$ (black cross) had a formation energy value equal to -2.01 eV; this value was between the ones corresponding to the $\text{Na}_{12}\text{Mn}_{11}\text{TiO}_{24}$ system (red cross; $E_f = -2.03$ eV) and to the $\text{Na}_{12}\text{Mn}_{11}\text{NiO}_{24}$ system (brown cross; $E_f = -1.93$ eV), respectively. The calculated values of the formation energy of

the $\text{Na}_{12}\text{Mn}_4\text{Ni}_4\text{Ti}_4\text{O}_{24}$ system (orange crosses) ranged from -1.98 to -1.94 eV. Finally, we list also the calculated E_f values for the systems in which two transition metals had the same concentration, i.e., $\text{Na}_{12}\text{Mn}_3\text{Ni}_6\text{Ti}_3\text{O}_{24}$ (magenta crosses; range from -1.80 to -1.77 eV), $\text{Na}_{12}\text{Mn}_6\text{Ni}_3\text{Ti}_3\text{O}_{24}$ (green crosses; range from -2.07 to -1.96 eV), and $\text{Na}_{12}\text{Mn}_4\text{Ni}_4\text{Ti}_4\text{O}_{24}$ (light blue crosses; range from -2.15 to -2.12 eV).

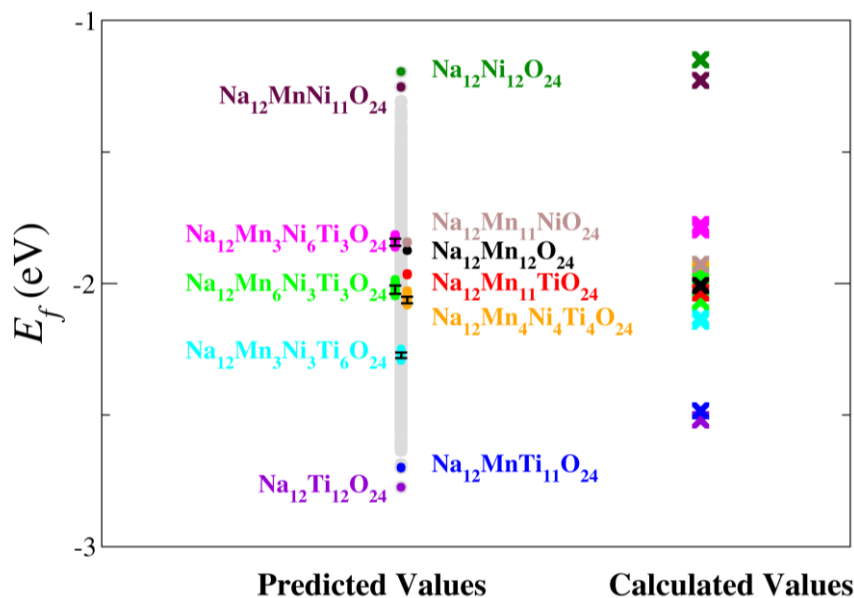


Figure 3. A comparison of the predicted (circles) and calculated (crosses) formation energy for the non-relaxed systems. For the $\text{Na}_{12}\text{Mn}_3\text{Ni}_6\text{Ti}_3\text{O}_{24}$, $\text{Na}_{12}\text{Mn}_6\text{Ni}_3\text{Ti}_3\text{O}_{24}$, $\text{Na}_{12}\text{Mn}_4\text{Ni}_4\text{Ti}_4\text{O}_{24}$, and $\text{Na}_{12}\text{Mn}_3\text{Ni}_3\text{Ti}_6\text{O}_{24}$ systems, the statistical uncertainty of the predicted formation energies is indicated by black solid lines centered in the mean values and limited by the standard deviations.

To further assess the predictive performance of the machine learning model, the predicted formation energies were compared against the calculated ones obtained through the DFT method managed by the AiiDA workflow. In this second stage, the DFT-calculated E_f was relative to that of the relaxed systems. Figure 4 shows the scatter plots of the predicted versus calculated formation energies for two sets of systems: the non-relaxed systems (red circles) are on panel (a) and the relaxed systems (blue circles) are on panel (b). Each data point represents a unique configuration of the material composition. As illustrated, most of the points lie close to the $y = x$ line (black dashed line), indicating a strong agreement between the predictions and the calculated values. The tight clustering around this line demonstrates the model's accuracy across a wide range of formation energies.

Furthermore, the accuracy of the predictions was quantified using the mean absolute error (MAE), the coefficient of determination (R^2), and Pearson's r correlation, as reported in Table 1. From the comparison of the scatter plots, two key observations emerge: (1) the GeoCGNN could provide reasonably accurate predictions for the formation energy using non-relaxed systems directly from the input CIF; (2) the accuracy improved for the relaxed systems, as indicated by the closer alignment of points with the diagonal in the plot of Figure 4b. The first observation is significant because we trained the DL model to make predictions while saving time, bypassing the need for computationally expensive first-principles calculations. The relaxed structure was only obtained after the calculation was complete (with both the formation energy and the relaxed structure as outputs). As far as we know, no DL models currently exist that could predict the geometry of the relaxed system. Therefore, the standard approach is to predict the formation energy of the non-relaxed crystal structure. Our results show that the GeoCGNN achieved satisfying accuracy in this task. The second observation is equally important, as the best performance of the predictive algorithms for relaxed systems agrees with the fact that Quantum Espresso

calculates the formation energy of relaxed structures. This is confirmation that the training of the GeoCGNN was successful.

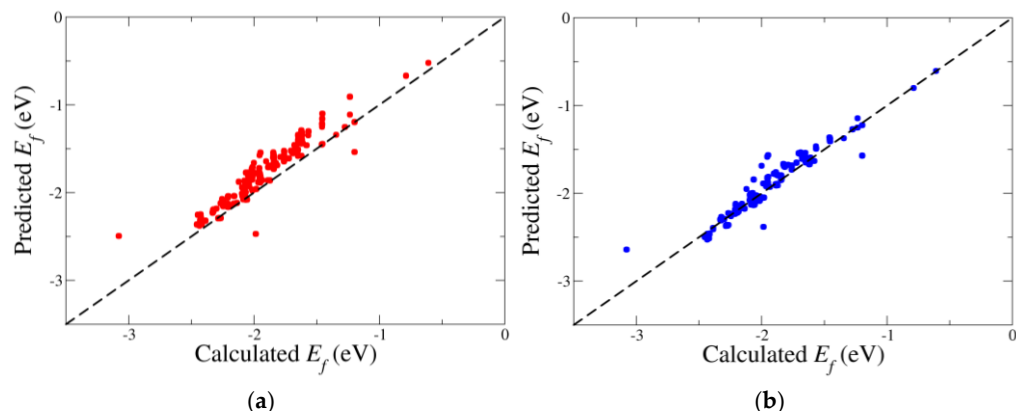


Figure 4. Scatter plots of the predicted vs. calculated formation energies, E_f , using non-relaxed (panel (a), red circles) and relaxed (panel (b), blue circles) systems. The black dashed line represents the ideal $y = x$ relationship.

Table 1. Mean absolute error (MAE), coefficient of determination (R^2), and Pearson's correlation coefficient (r) were calculated by comparing predicted and calculated formation energies for non-relaxed and relaxed systems.

Systems	MAE (eV)	R^2	Pearson's r
Non-relaxed	0.166	0.665	0.960
Relaxed	0.052	0.944	0.975

4. Conclusions

In conclusion, to evaluate the stability of substitutionally doped P2-layered oxide NaMnO_2 cathode materials, we adopted two different computational methods: (1) computationally demanding, high-throughput, first-principles DFT calculations; and (2) an ML technique based on the training of a GeoCGNN. In both cases, we explored a wide combinatorial space of material candidates for cathode batteries by generating numerous alternative compositions through the random substitution of Mn atoms. The DFT calculations were automated and integrated into a computational workflow chain developed within the AiiDA framework. The first-principles total energy of the materials was used to evaluate the formation energy. On the other hand, we adopted a data-driven approach where the GeoCGNN was used to predict the formation energy as the target property of the generated crystals upon training on a dataset extracted from the Materials Project database [19]. The input of the GeoCGNN model was a graph supplemented with other information on the crystal lattice. The results revealed that titanium doping improved the system's stability, while nickel doping reduced it.

To evaluate the predictive performance of the DL model, the predicted formation energies were compared to the calculated formation energies obtained from DFT calculations. Our results show that the GeoCGNN achieved satisfying accuracy in predicting the formation energy of non-relaxed crystal structures, with the accuracy improving when relaxed systems were used as the input. This demonstrates that the GeoCGNN was successfully trained to predict results consistent with the DFT calculations, which computed the formation energy of the relaxed structures. However, since the relaxed structures were only available after performing the DFT total energy calculation, the most effective approach without executing DFT calculations was to use the non-relaxed systems as the input for the GeoCGNN to generate predictions.

To further enhance the ML model and expand its applicability, the model's versatility can be improved by incorporating properties such as the band gap, the bulk modulus, the shear modulus, and Poisson's ratio into the training dataset. These properties often correlate with critical performance metrics, such as mechanical stability and electronic characteristics, thereby improving the understanding of material behavior. Additionally, by reusing a pre-trained ML model, such as one developed for predicting electronic properties, it may be possible to fine-tune the model for other related properties, like redox potential, using transfer learning for cross-property prediction techniques. This approach could significantly reduce computational resource requirements while leveraging existing knowledge.

The Hubbard correction improves the description of the d-orbitals correlation in transition metal electronic shells and the energy gap estimation. However, the r2SCAN meta-GGA exchange–correlation functional [43] performs better than GGA in predicting the thermodynamic properties of various 3d, 4d, and 5d transition metals [44]. Therefore, the adoption of the r2SCAN functional in workflows is a promising strategy for future research.

As final observation, it is worth noting that running a typical DFT calculation for a single crystal structure requires a time ranging from 1 to 24 h, while training the model from the dataset requires a few hours, and a single prediction is made in fractions of a second. This demonstrates that the GeoCGNN reduces the time required to predict material properties by several orders of magnitude compared to traditional DFT calculations, while maintaining satisfactory accuracy. Additionally, the reduction in energy consumption is significant and should not be overlooked.

Author Contributions: Conceptualization, F.B.; methodology, F.B., C.R., and S.G.; software, C.R. and S.F.; validation, S.G., F.B., S.M., and C.R.; investigation, C.R., S.M., F.B., S.G., and M.C.; resources, M.C.; data curation, C.R. and S.F.; writing—original draft preparation, C.R., S.M., S.G., and F.B.; writing—review and editing, F.B. and S.G.; supervision, F.B. and M.C.; project administration, M.C.; funding acquisition, M.C. All authors have read and agreed to the published version of the manuscript.

Funding: The Project “Italian Energy Materials Acceleration Platform” (IEMAP)—CUP I62C21000380001 in the Program Mission Innovation is acknowledged for financial support. This work was supported by the European Union through the Next Generation EU funds through the Italian MUR National Recovery and Resilience Plan, Mission 4 Component 2—Investment 1.4—National Center for HPC, Big Data and Quantum Computing—CUP I33C22001270007.

Data Availability Statement: The dataset generated in this study is available at <https://iemap.enea.it/> (accessed on 2 December 2024). The code used for this study is available at <https://gitlab.brindisi.enea.it/claudio.ronchetti/ai4mat> (accessed on 2 December 2024).

Acknowledgments: The computing resources and the related technical support used for this work were provided by the CRESCO/ENEAGRID High-Performance Computing infrastructure and its staff [34]. The CRESCO/ENEAGRID High-Performance Computing infrastructure is funded by ENEA, the Italian National Agency for New Technologies, Energy and Sustainable Economic Development and by Italian and European research projects; see <http://www.cresco.enea.it/english> (accessed on 30 April 2024) for information. The authors acknowledge the extensive use of the ENEA FARO facility and the support of its management team [45].

Conflicts of Interest: Author Claudio Ronchetti was employed by the company Telespazio S.p.A. The remaining authors declare that the research was conducted in the absence of any commercial or financial relationships that could be construed as a potential conflict of interest.

References

1. Bhuiyan, M.R.A. Overcome the future environmental challenges through sustainable and renewable energy resources. *Micro Nano Lett.* **2022**, *17*, 402–416. [[CrossRef](#)]
2. Chakraborty, A.; Kunnikuruvan, S.; Kumar, S.; Markovsky, B.; Aurbach, D.; Dixit, M.; Major, D.T. Layered Cathode Materials for Lithium-Ion Batteries: Review of Computational Studies on $\text{LiNi}_{1-x-y}\text{Co}_x\text{Mn}_y\text{O}_2$ and $\text{LiNi}_{1-x-y}\text{Co}_x\text{Al}_y\text{O}_2$. *Chem. Mater.* **2020**, *32*, 915–952. [[CrossRef](#)]
3. Kim, S.-W.; Seo, D.-H.; Ma, X.; Ceder, G.; Kang, K. Electrode Materials for Rechargeable Sodium-Ion Batteries: Potential Alternatives to Current Lithium-Ion Batteries. *Adv. Energy Mater.* **2012**, *2*, 710–721. [[CrossRef](#)]

4. Clement, R.J.; Bruce, P.G.; Grey, C.P. Review—Manganese-Based P2-Type Transition Metal Oxides as Sodium-Ion Battery Cathode Materials. *J. Electrochem. Soc.* **2015**, *162*, A2589. [[CrossRef](#)]
5. Liu, Q.; Hu, Z.; Chen, M.; Zou, C.; Jin, H.; Wang, S.; Chou, S.-L.; Dou, S.-X. Recent Progress of Layered Transition Metal Oxide Cathodes for Sodium-Ion Batteries. *Small* **2019**, *15*, 1805381. [[CrossRef](#)]
6. Zhang, J.; Wang, W.; Wang, W.; Wang, S.; Li, B. Comprehensive Review of P2-Type $\text{Na}_{2/3}\text{Ni}_{1/3}\text{Mn}_{2/3}\text{O}_2$, a Potential Cathode for Practical Application of Na-Ion Batteries. *ACS Appl. Mater. Interfaces* **2019**, *11*, 22051–22066. [[CrossRef](#)]
7. Rostami, H.; Valio, J.; Suominen, P.; Tynjälä, P.; Lassi, U. Advancements in Cathode Technology, Recycling Strategies, and Market Dynamics: A Comprehensive Review of Sodium Ion Batteries. *Chem. Eng. J.* **2024**, *495*, 153471. [[CrossRef](#)]
8. Lee, D.H.; Xu, J.; Meng, Y.S. An advanced cathode for Na-ion batteries with high rate and excellent structural stability. *Phys. Chem. Chem. Phys.* **2013**, *15*, 3304–3312. [[CrossRef](#)]
9. Prosini, P.P.; Carewska, M.; Cento, C.; Tarquini, G.; Maroni, F.; Birrozzzi, A.; Nobili, F. Tin-Decorated Reduced Graphene Oxide and $\text{NaLi}_{0.2}\text{Ni}_{0.25}\text{Mn}_{0.75}\text{O}_8$ as Electrode Materials for Sodium-Ion Batteries. *Materials* **2019**, *12*, 1074. [[CrossRef](#)]
10. Sun, Y.-K.; Jeon, Y.-S.; Leeb, H.J. Overcoming Teller-Teller Distortion for Spinel Mn Phase. *Electrochem. Solid-State Lett.* **1999**, *3*, 7–9. [[CrossRef](#)]
11. Thackeray, M.M. Manganese oxides for lithium batteries. *Prog. Solid State Chem.* **1997**, *25*, 1–71. [[CrossRef](#)]
12. Gupta, P.; Pushpakanth, S.; Ali Haider, M.; Basu, S. Understanding the Design of Cathode Materials for Na-Ion Batteries. *ACS Omega* **2022**, *7*, 5605–5614. [[CrossRef](#)] [[PubMed](#)]
13. Nguyen, T.P.; Kim, I.T. Recent Advances in Sodium-Ion Batteries: Cathode Materials. *Materials* **2023**, *16*, 6869. [[CrossRef](#)] [[PubMed](#)]
14. Wang, H.; Gao, X.; Zhang, S.; Mei, Y.; Ni, L.; Gao, J.; Liu, H.; Hong, N.; Zhang, B.; Zhu, F.; et al. High-Entropy Na-Deficient Layered Oxides for Sodium-Ion Batteries. *ACS Nano* **2023**, *17*, 12530–12543. [[CrossRef](#)] [[PubMed](#)]
15. Yoshida, H.; Yabuuchi, N.; Kubota, K.; Ikeuchi, I.; Garsuch, A.; Schulz-Dobrick, M.; Komaba, S. P2-Type $\text{Na}_{2/3}\text{Ni}_{1/3}\text{Mn}_{2/3-x}\text{T}_{x}\text{O}_2$ as a New Positive Electrode for Higher Energy Na-Ion Batteries. *Chem. Commun.* **2014**, *50*, 3677–3680. [[CrossRef](#)]
16. Cao, Z.; Li, L.; Zhou, C.; Ma, X.; Wang, H. Contribution of titanium substitution on improving the electrochemical properties of P2- $\text{Na}_{0.67}\text{Ni}_{0.33}\text{Mn}_{0.67}\text{O}_2$ cathode material for sodium-ion storage. *Funct. Mater. Lett.* **2020**, *13*, 2051010.
17. Lombardo, T.; Duquesnoy, M.; El-Bouysidy, H.; Åren, F.; Gallo-Bueno, A.; Bjørn Jørgensen, P.; Bhowmik, A.; Demortière, A.; Ayerbe, E.; Alcaide, F.; et al. Artificial Intelligence Applied to Battery Research: Hype or Reality? *Chem. Rev.* **2022**, *122*, 10899–10969. [[CrossRef](#)]
18. Ronchetti, C.; Puccini, M.; Ferlito, S.; Giusepponi, S.; Palombi, F.; Buonocore, F.; Celino, M. Machine learning techniques for data analysis in materials science. In Proceedings of the 2022 AEIT International Annual Conference (AEIT), Rome, Italy, 3–5 October 2022; pp. 1–6. [[CrossRef](#)]
19. Jain, A.; Ping Ong, S.; Hautier, G.; Wei, C.; Richards, W.D.; Dacek, S.; Cholia, S.; Gunter, D.; Skinner, D.; Ceder, G.; et al. Commentary: The Materials Project: A materials genome approach to accelerating materials innovation. *APL Mater.* **2013**, *1*, 011002. [[CrossRef](#)]
20. Giannozzi, P.; Baroni, S.; Bonini, N.; Calandra, M.; Car, R.; Cavazzoni, C.; Ceresoli, D.; Chiarotti, G.L.; Cococcioni, M.; Dabo, I.; et al. QUANTUM ESPRESSO: A modular and open-source software project for quantum simulations of materials. *J. Phys.* **2009**, *21*, 39502. [[CrossRef](#)]
21. Giannozzi, P.; Andreussi, O.; Brumme, T.; Bunau, O.; Nardelli, M.B.; Calandra, M.; Car, R.; Cavazzoni, C.; Ceresoli, D.; Cococcioni, M.; et al. Advanced capabilities for materials modelling with Quantum ESPRESSO. *J. Phys. Condens. Matter* **2017**, *29*, 465901. [[CrossRef](#)]
22. Hohenberg, P.; Kohn, W. Inhomogeneous electron gas. *Phys. Rev.* **1964**, *136*, B864. [[CrossRef](#)]
23. Kohn, W.; Sham, L.J. Self-consistent equations including exchange and correlation effects. *Phys. Rev.* **1965**, *140*, A1133. [[CrossRef](#)]
24. Perdew, J.P.; Burke, K.; Ernzerhof, M. Generalized gradient approximation made simple. *Phys. Rev. Lett.* **1996**, *77*, 3865–3868. [[CrossRef](#)] [[PubMed](#)]
25. Monkhorst, H.J.; Pack, J.D. Special points for Brillouin-zone integrations. *Phys. Rev. B* **1976**, *13*, 5188. [[CrossRef](#)]
26. Marzari, N.; Vanderbilt, D.; De Vita, A.; Payne, M.C. Thermal contraction and disordering of the Al(110) surface. *Phys. Rev. Lett.* **1999**, *82*, 3296. [[CrossRef](#)]
27. Himmetoglu, B.; Floris, A.; Gironcoli, S.; Cococcioni, M. Hubbard-corrected DFT energy functionals: The LDA+U description of correlated systems. *Int. J. Quantum Chem.* **2014**, *114*, 14–49. [[CrossRef](#)]
28. Pizzi, G.; Cepellotti, A.; Sabatini, R.; Marzari, N.; Kozinsky, B. AiiDA: Automated interactive infra-structure and database for computational science. *Comput. Mater. Sci.* **2016**, *111*, 218–230. [[CrossRef](#)]
29. Huber, S.P.; Zoupanos, S.; Uhrin, M.; Talirz, L.; Kahle, L.; Häuselmann, R.; Gresch, D.; Müller, T.; Yakutovich, A.V.; Andersen, C.W.; et al. AiiDA 1.0, a scalable computational infrastructure for automated reproducible workflows and data provenance. *Sci. Data* **2020**, *7*, 300. [[CrossRef](#)]
30. Uhrin, M.; Huber, S.P.; Yu, J.; Marzari, N.; Pizzi, G. Workflows in AiiDA: Engineering a high-throughput, event-based engine for robust and modular computational workflows. *Comput. Mater. Sci.* **2021**, *187*, 110086. [[CrossRef](#)]
31. Available online: <https://github.com/aiidateam/aiida-quantumespresso> (accessed on 30 April 2023).
32. Lonie, D.; Zurek, E. Identifying duplicate crystal structures: XTALCOMP, an open-source solution. *Comput. Phys. Commun.* **2012**, *183*, 690–697. [[CrossRef](#)]

33. Larsen, A.H.; Mortensen, J.J.; Blomqvist, J.; Castelli, I.E.; Christensen, R.; Dułak, M.; Friis, J.; Groves, M.N.; Hammer, B.; Hargus, C.; et al. The atomic simulation environment—A Python library for working with atoms. *J. Phys. Condens. Matter* **2017**, *29*, 273002. [[CrossRef](#)]
34. Iannone, F.; Ambrosino, F.; Bracco, G.; De Rosa, M.; Funel, A.; Guarneri, G.; Migliori, S.; Palombi, F.; Ponti, G.; Santomauro, G.; et al. CRESCO ENEA HPC clusters: A working example of a multi-fabric GPFS Spectrum Scale layout. In Proceedings of the 2019 International Conference on High Performance Computing & Simulation (HPCS), Dublin, Ireland, 15–19 July 2019; pp. 1051–1052.
35. Cheng, J.; Zhang, C.; Dong, L. A geometric-information-enhanced crystal graph network for predicting properties of materials. *Commun. Mater.* **2021**, *2*, 92. [[CrossRef](#)]
36. Xie, T.; Grossman, J.C. Crystal graph convolutional neural networks for an accurate and interpretable prediction of material properties. *Phys. Rev. Lett.* **2018**, *120*, 145301. [[CrossRef](#)] [[PubMed](#)]
37. Gilmer, J.; Schoenholz, S.S.; Riley, P.F.; Vinyals, O.; Dahl, G.E. Neural message passing for quantum chemistry. In Proceedings of the 34th International Conference on Machine Learning, Sydney, Australia, 6–11 August 2017; PMLR, Volume 70, pp. 1263–1272.
38. Weil, S.A.; Brandt, S.A.; Miller, E.L.; Long, D.D.; Maltzahn, C. Ceph: A scalable, high-performance distributed file system. In Proceedings of the 7th Conference on Operating Systems Design and Implementation (OSDI ‘06), Seattle, WA, USA, 6–8 November 2006; pp. 307–320.
39. Amari, S.I. Backpropagation and stochastic gradient descent method. *Neurocomputing* **1993**, *5*, 185–196. [[CrossRef](#)]
40. Goodfellow, I.; Bengio, Y.; Courville, A. *Deep Learning*; MIT Press: Cambridge, MA, USA, 2016.
41. Géron, A. *Hands-On Machine Learning with Scikit-Learn, Keras, and TensorFlow*, 2nd ed.; O’Reilly Media: Sebastopol, CA, USA, 2019.
42. Bishop, C.M. *Pattern Recognition and Machine Learning*; Springer: Berlin/Heidelberg, Germany, 2006.
43. Furness, J.W.; Kaplan, A.D.; Ning, J.; Perdew, J.P.; Sun, J. Accurate and Numerically Efficient r2SCAN Meta-Generalized Gradient Approximation. *J. Phys. Chem. Lett.* **2020**, *11*, 8208–8215. [[CrossRef](#)]
44. Kothakonda, M.; Kaplan, A.D.; Isaacs, E.B.; Bartel, C.J.; Furness, J.W.; Ning, J.; Wolverton, C.; Perdew, J.P.; Sun, J. Testing the r2SCAN Density Functional for the Thermodynamic Stability of Solids with and without a van der Waals Correction. *ACS Mater. Au* **2023**, *3*, 102–111. [[CrossRef](#)]
45. Mariano, A.; D’amato, G.; Ambrosino, F.; Aprea, G.; Buonocore, F.; Celino, M.; Colavincenzo, A.; Fina, M.; Funel, A.; Giusepponi, S.; et al. Fast Access to Remote Objects 2.0 a renewed gateway to ENEAGRID distributed computing resources. *Future Gener. Comput. Syst.* **2019**, *94*, 920–928. [[CrossRef](#)]

Disclaimer/Publisher’s Note: The statements, opinions and data contained in all publications are solely those of the individual author(s) and contributor(s) and not of MDPI and/or the editor(s). MDPI and/or the editor(s) disclaim responsibility for any injury to people or property resulting from any ideas, methods, instructions or products referred to in the content.